Paleoceanography and Paleoclimatology

RESEARCH ARTICLE
10.1029/2026PA005506

Low Chemical Weathering Intensity, Enhanced Erosion, and Euxinic Conditions Along the Norwegian Margin During the Paleocene-Eocene Thermal Maximum

Anjana Gireesh Sandhya[1], Jack Longman[2], Torben Struve[1], Morgan T. Jones[3,4], Joost Frieling[5,6], and Katharina Pahnke[1]

[1]Institute for Chemistry and Biology of the Marine Environment (ICBM), Carl von Ossietzky Universität Oldenburg, Oldenburg, Germany, [2]Department of Geography and Environmental Sciences, Northumbria University, Newcastle, UK, [3]Department of Ecology, Environment and Geoscience (EMG), Umeå University, Umeå, Sweden, [4]Department of Geosciences, University of Oslo, Oslo, Norway, [5]Department of Earth Sciences, University of Oxford, Oxford, UK, [6]Department of Geology, Ghent University, Ghent, Belgium

Key Points:

- Physical erosion dominant weathering style on the mid Norwegian margin during the Paleocene Eocene Thermal Maximum
- Bottom waters in the Vøring Basin became euxinic at the onset of this warming event
- Strong physical erosion linked to the development of oxygen poor and sulfur rich conditions offshore

Supporting Information:

Supporting Information may be found in the online version of this article.

Correspondence to:

A. G. Sandhya,
anjana.gireesh.sandhya@uni-oldenburg.de

Citation:

Sandhya, A. G., Longman, J., Struve, T., Jones, M. T., Frieling, J., & Pahnke, K. (2026). Low chemical weathering intensity, enhanced erosion, and euxinic conditions along the Norwegian margin during the Paleocene-Eocene thermal maximum. *Paleoceanography and Paleoclimatology*, *41*, e2026PA005506. https://doi.org/10.1029/2026PA005506

Received 6 APR 2026
Accepted 19 JUN 2026

Author Contributions:

Conceptualization: Anjana Gireesh Sandhya, Jack Longman
Data curation: Anjana Gireesh Sandhya
Formal analysis: Anjana Gireesh Sandhya
Funding acquisition: Jack Longman
Investigation: Anjana Gireesh Sandhya, Jack Longman
Methodology: Anjana Gireesh Sandhya, Jack Longman
Project administration: Jack Longman, Katharina Pahnke
Resources: Katharina Pahnke
Supervision: Jack Longman, Katharina Pahnke
Visualization: Anjana Gireesh Sandhya, Jack Longman

Abstract The Paleocene–Eocene Thermal Maximum (PETM; ~55.9 Ma) was a rapid global warming event marked by intensified hydrological cycling, enhanced continental weathering, and widespread ocean deoxygenation. Although the extent of anoxic basins during the PETM is relatively well documented, the contribution of high-latitude continental weathering to regional ocean redox dynamics remains unclear, leaving the spatial impact of weathering on ocean biogeochemistry poorly constrained. Here, we use elemental geochemical data from sediments recovered from the Vøring Basin, North Atlantic during International Ocean Discovery Program (IODP) Expedition 396, to reconstruct variations in continental weathering intensity and redox conditions across the PETM. Our results show that high accumulation rates during the PETM coincided with low chemical weathering relative to underlying pre-PETM strata, indicating that rapid burial limited chemical alteration, although accumulation rates in the pre-PETM interval are not well constrained. This pattern likely reflects intensified rainfall, which primarily enhanced physical erosion and delivered large amounts of detrital material to the basin while limiting chemical weathering. The influx of fresh, reactive detrital material from the North Atlantic Igneous Province (NAIP) increased the supply of bioavailable nutrients, likely stimulating elevated primary productivity and contributing to the development of euxinic bottom waters during the onset of the PETM. On the boreal mid-Norwegian margin, our data suggest that enhanced physical erosion, rather than chemical weathering, dominated continental responses to extreme greenhouse forcing, promoting nutrient enrichment, transient euxinia, and organic carbon burial.

Plain Language Summary About 56 million years ago, the Earth experienced rapid global warming during the Paleocene-Eocene Thermal Maximum (PETM). Increased rainfall caused intense physical erosion on land, delivering large amounts of sediment to the Vøring Basin on the mid-Norwegian margin. Most erosion was physical rather than chemical, and the influx of nutrient-rich material likely boosted ocean productivity. This led to temporary oxygen-poor, sulfur-rich (euxinic) conditions on the seafloor. Our study shows that high-latitude land erosion played a key role in shaping regional ocean chemistry and carbon burial during this extreme warming event. These results highlight how continental processes can directly influence ocean conditions during rapid climate change.

1. Introduction

The Paleocene-Eocene Thermal Maximum (PETM) was a rapid global warming event which commenced 55.93 ± 0.1 million years ago (Ma) (Charles et al., 2011; Jones et al., 2025; Westerhold et al., 2007; Zeebe & Lourens, 2019) and lasted for ≥200 ka (Röhl et al., 2007). It is characterized by the rapid and voluminous input of $\delta^{13}C$ depleted carbon into the atmosphere and ocean, causing a 2‰–7‰ negative carbon isotope excursion (CIE) (McInerney & Wing, 2011), and a rise in global sea surface temperature by ~5°C (Dunkley Jones et al., 2013; Frieling et al., 2017; Tierney et al., 2022). The onset and main phase (also referred to as "body" or "plateau") of the PETM are commonly estimated at ~170 ka (Jones et al., 2025; Longman, Gernon, et al., 2021; Zeebe & Lourens, 2019) whereas the full duration of the CIE, including the extended recovery, may have been substantially longer up to ~269 ka (Piedrahita et al., 2025).

Writing – original draft: Anjana Gireesh Sandhya
Writing – review & editing: Anjana Gireesh Sandhya, Jack Longman, Torben Struve, Morgan T. Jones, Joost Frieling, Katharina Pahnke

The intrusion of igneous material associated with the North Atlantic Igneous Province (NAIP) into organic-rich sedimentary basins, which lead to thermogenic methane and CO_2 release, is considered as a major carbon source contributing to the PETM CIE (Berndt et al., 2023; Frieling et al., 2016; Jones et al., 2019; Svensen et al., 2004). Geophysical observations have identified over 700 potential hydrothermal vent complexes (HTVCs) of early Eocene age linked with this methane release along the mid-Norwegian margin alone (Planke et al., 2005). International Ocean Discovery Program (IODP) Expedition 396 drilled into the sedimentary sequence of one such HTVC, providing new constraints on the timing and evolution of magmatism and associated hydrothermal vent systems across the Paleocene–Eocene transition (Planke et al., 2023). This work also indicated the (very) shallow marine setting in which these HTVCs were active in the northern North Atlantic (Berndt et al., 2023).

The PETM is linked to various environmental and climatic changes including an enhanced hydrological cycle (Carmichael et al., 2017; Handley et al., 2012). Enhanced moisture transport and increased precipitation during the PETM led to both intensified silicate weathering and a significant rise in global sediment erosion rates (Penman et al., 2019; Pogge von Strandmann et al., 2021). Furthermore, high concentrations of kaolinite, a product of chemical weathering in warm, wet climate, have been observed during the PETM in many marginal marine sites around the world (Bolle & Adatte, 2001; Chen et al., 2016; Robert & Kennett, 1994). However, much of this kaolinite likely represents deposition of pre-existing, deeply weathered soils and bedrocks, emphasizing the role of physical erosion and sediment transport (John et al., 2012; Pujalte et al., 2015; Rush et al., 2025; Stokke et al., 2021). The changes in (hydro-)climate also appear to have had a profound large-scale impact on vegetation (Korasidis et al., 2022) and a transient reduction in vegetation cover such as reconstructed for mid- and high-latitudes (Nelissen et al., 2026) may have influenced erosion patterns. At a broader scale, these processes are part of the silicate weathering continuum from mountains to the deep ocean that regulates global alkalinity and atmospheric CO_2, linking terrestrial weathering and erosion to changes in ocean chemistry and long-term climate (Trapp-Müller et al., 2025).

Ocean warming, higher nutrient input, increased water column stratification, and the oxidation of a large reservoir of stored carbon are all thought to have played a role in affecting marine oxygen concentrations. The magnitude of deoxygenation likely varied depending on local environmental factors in the southern Atlantic (Chang et al., 2018; Remmelzwaal et al., 2019; Winguth et al., 2012), north-eastern Atlantic and northern Pacific (Remmelzwaal et al., 2019), Peri-Tethys (Dickson et al., 2014), and the Arctic Ocean (Cohen & Coe, 2012). Shallow shelf seas such as around the Tethys, semi-enclosed basins (Arctic, North Atlantic) and epicontinental seaways recorded the most severe anoxia, including local to regional scale photic zone euxinia (Behrooz et al., 2024; Kaya et al., 2022; Papadomanolaki et al., 2022; Schoon et al., 2015; Stokke et al., 2021).

Despite data from some PETM sites suggesting both high weathering rates and low oceanic oxygen levels, it remains unclear how globally representative these patterns were or whether the drivers of deoxygenation varied spatially. The high-resolution sedimentary archive recovered from the Norwegian Margin provides an opportunity to examine climatic and oceanographic changes during the PETM at unprecedented temporal detail. In this study, we use a suite of geochemical proxies to investigate variations in weathering intensity and basin oxygenation across the PETM, compare these to pre- and post-PETM conditions, and assess the relative roles of chemical versus physical weathering in driving deoxygenation.

2. Materials and Methods

2.1. Site Description

The samples used for the study were collected during IODP Expedition 396 from the mid-Norwegian margin, with core location and sampling details reported in Planke et al. (2023). Five boreholes were drilled through the Modgunn HTVC crater, recovering infill sediments and sub-vent strata. The boreholes are listed here in order of proximity to the vent center: Holes U1568A, U1568B, U1567B, U1567C, and U1567A (Figure 1)). From bottom to top, the succession begins with greenish mudstones of Unit VI, late Paleocene in age, containing *Alisocysta margarita* (Berndt et al., 2023). The vent infill comprises Units V and IV: Unit V is very dark, parallel-laminated claystone with sub-millimeter diatomite laminae and no bioturbation, reflecting largely undisturbed deposition, whereas Unit IV consists of dark greenish-gray to very dark gray claystone and siltstone with ash and minor bioturbation, reflecting rapid, minimally reworked deposition (Planke et al., 2023). Ash layers distributed throughout the vent infill indicate largely undisturbed accumulation of volcaniclastic material during sustained surface or shallow-water explosive volcanism (Vickers et al., 2024). The PETM interval is marked by the

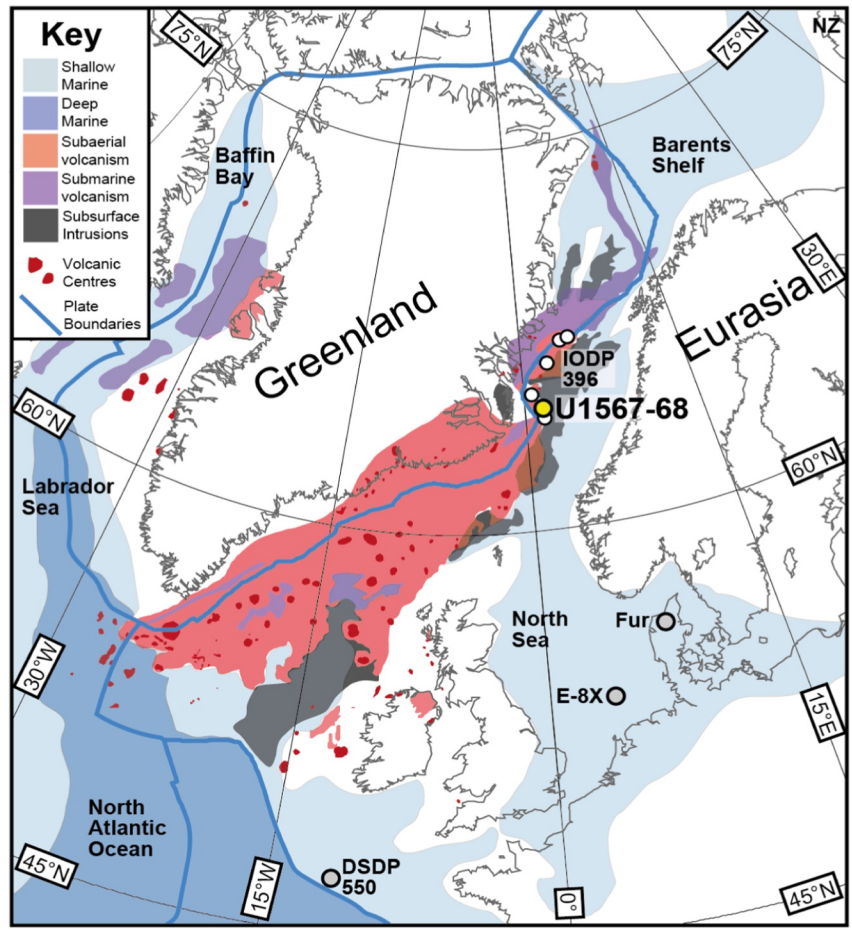

Figure 1. Paleoceanographic plate reconstruction at 56 Ma illustrating the North Sea region with NAIP volcanism, modified after Jones et al. (2023). The study area on the mid-Norwegian margin is highlighted by a yellow circle. Key sites of PETM reconstructions discussed in this work are: E-8X from the North Sea (Mariani et al., 2024), outcrops on the island of Fur, Denmark (Jones et al., 2019), and DSDP Site 550 in the North Atlantic (Knox, 1984).

occurrence of *Apectodinium augustum* and a sharp ~6‰ negative $\delta^{13}C_{org}$ shift near the base (Figure 3), followed by a ~2‰ negative excursion relative to pre-PETM strata up section. Overlying units are considerably younger, indicating an unconformity above Unit IV of >5 Myr duration that postdates doming of the vent infill strata (Planke et al., 2023).

We focus here on the stratigraphically most expanded Hole U1568A, while noting subtle differences across the five-hole transect. At U1568A, the transition between lithostratigraphic Unit VI and Unit V coincides with the onset of the CIE. However, near the vent center, the section is condensed or partly missing, likely due to vent-related processes such as collapse or blow-out events. This local hiatus resulted in the absence of the latest Paleocene part of Unit V at site U1568A. This is in contrast to its preservation at site U1567B, indicating a localized stratigraphic hiatus at the vent center. We use the first occurrence of the dinocyst *Apectodinium augustum* (at the Unit VI-V boundary) and corresponding negative δ^{13}Corg values (<−30‰) to mark the base of the preserved PETM record at U1568A. This is further supported by the co-occurrence of the first occurrence of *A. augustum* and CIE onset at U1567B. In contrast, at Holes U1567A–C, several meters of latest Paleocene sediment separate the unit boundary from the CIE onset. Fewer carbon isotope data are available for the U1568B record but combined with patterns in lithology (fine laminations) and magnetic susceptibility the onset of the PETM interval in U1568B likely sits above the VI-V boundary, around *ca.* 96 m below seafloor (mbsf) with the unit VI-V boundary at 103.87 mbsf, (Berndt et al., 2023; Planke et al., 2023). However, given the presence of the unconformity at U1568A, part of the earliest PETM interval, including the CIE onset, may not be fully preserved in Hole U1568A.

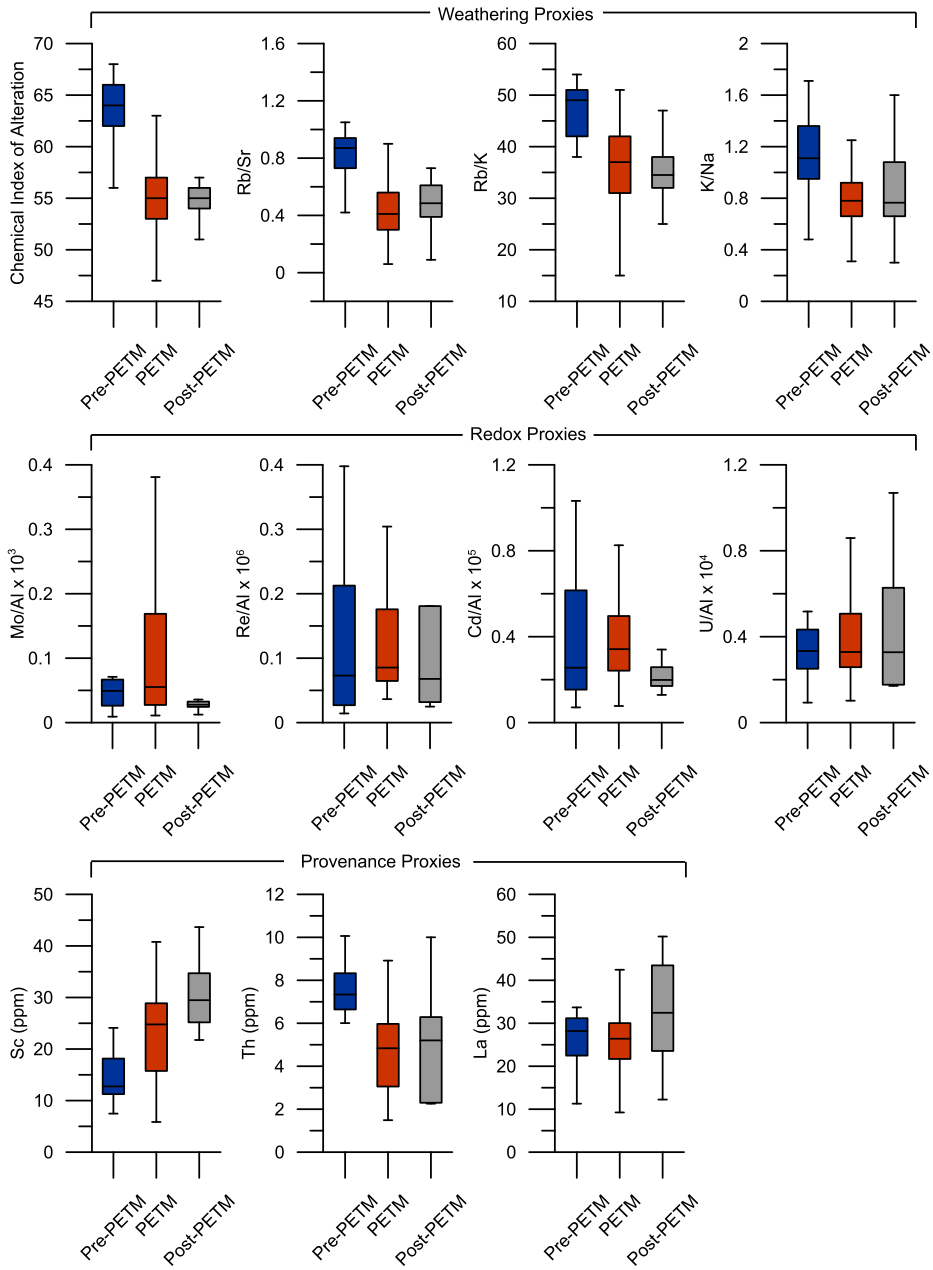

Figure 2. Box plots show geochemical proxy distributions across pre-PETM, PETM, and post-PETM intervals. Weathering proxies (Hole U1568A) include CIA, Rb/Sr, Rb/K, and K/Na. Redox-sensitive proxies (Hole U1568A) include Mo/Al, Re/Al, Cd/Al, and U/Al. Provenance proxies include La, Th, and Sc from Holes U1568A–B and U1567B. The solid black line in each box plot denotes the median. Boxes represent the interquartile range (25th–75th percentiles), with whiskers extending to 1.5 × IQR. Outliers beyond this range are not shown.

2.2. Geochemical Analyses

The elemental composition of all core samples was analyzed at the Institute for Chemistry and Biology of the Marine Environment (ICBM), Oldenburg, Germany. Prior to analysis, all samples were freeze dried and homogenized using an agate ball mill.

2.2.1. XRF Analysis

Major and trace elemental compositions were determined using a Wavelength Dispersive X-Ray Fluorescence Spectrometer (WD-XRF, Panalytical Axios Plus) following published procedures (Böning et al., 2004). In brief, about 700 mg of sample was mixed with 4,200 mg of dilithiumtetraborate and 1,000 mg of ammonium nitrate before heating to 1,150°C. The samples melted and were cast into a mold with a flat bottom resulting in the formation of a fused glass bead. Quality control of measurements was performed using the in-house reference material PS-S (Posidonia-shale) and certified reference material SDO-1 (Devonian Ohio Shale), for analytical trueness and precision. The RSD (relative standard deviation) is a measure of analytical precision, calculated as (standard deviation/mean) × 100, while trueness represents the percentage deviation from certified reference values. In general, trueness and RSD values of ≤5% are considered excellent for major elements while values ≤10% are typically acceptable for minor and trace elements due to lower concentrations and higher analytical uncertainty. For the major elements Al_2O_3, CaO, K_2O, and Na_2O, both trueness and RSD were below 5% for both reference materials, except for K_2O, which showed a trueness of 7%. For the minor oxide P_2O_5 and the trace elements rubidium (Rb) and strontium (Sr), trueness and RSD were ≤7% (Figure 3).

2.2.2. TQ ICP-MS Analysis

The trace and rare earth element (REE) concentrations of the samples were determined using a Thermo Scientific™ iCap Triple-Quadrupole Inductively-Coupled Plasma Mass Spectrometer (TQ-ICP-MS). Approximately 50 mg of freeze-dried sample was placed into a clean polytetrafluorethylene (PTFE) beaker. Based on XRF measurements indicating elevated Al_2O_3 contents (~13 wt%), magnesium (Mg) was added as magnesium oxide (MgO) to the sample prior to digestion to increase the (Mg + Ca)/Al ratio to suppress the formation of insoluble aluminum fluoride (AlF_3) and thereby improve trace-element recoveries (Takei et al., 2001). Subsequently, 1 mL of self-distilled concentrated nitric acid (HNO_3) was added to oxidize organic matter, carbonates, and sulfides. The mixture was then heated on a hotplate at 130°C for 2 hr. Subsequently, 3 mL of concentrated hydrofluoric acid (HF) and 0.5 mL of perchloric acid ($HClO_4$) were added, both of commercially obtained suprapure grade (Merck). The samples were capped and then heated in an oven at 180°C for at least 6 hours. After digestion, the acids were evaporated on a hotplate at 180°C until near dryness. The remaining residues were dissolved three times in 3 mL of 6 M hydrochloric acid (HCl), prepared from self-distillated of p.a grade acid, with each cycle fumed to near dryness. Finally, the residues were re-dissolved in 6 mL of single-distilled concentrated HNO_3 and diluted to a final volume of 25 mL using 2% HNO_3, yielding a final solution matrix of 2% HNO_3 for analysis. Certified reference materials SDO-1 and BE-N (basalt), in-house reference material DR-BS (black shale) and procedural blanks were prepared in the same manner. The trueness and precision of elements molybdenum (Mo), uranium (U), rhenium (Re) (Figure 3), lanthanum (La), thorium (Th), and scandium (Sc) (Figure 4) were <10%. Cadmium (Cd) showed acceptable precision (RSD = 2.92%) for DR-BS, with trueness slightly greater than ±10% (11%), but larger deviations occurred in other reference materials; therefore, only qualitative information is reported for this element. The procedural blanks for all elements were below 1% so no blank correction was applied.

2.2.3. Chemical Index of Alteration (CIA) Calculation

The Chemical Index of Alteration (CIA) was calculated following (McLennan et al., 1993; Nesbitt & Young, 1984) using molar proportions of Al_2O_3, CaO*, Na_2O, and K_2O. Cao* represents CaO in the silicate fraction and not CaO present in apatite and carbonate (Fedo et al., 1995). The correction procedure for CaO* follows McLennan et al. (1993): CaO is first corrected for apatite using P_2O_5 data ($CaO' = CaO - 10/3 \times P_2O_5$), and then CaO* is set equal to Na_2O if CaO′ exceeds Na_2O, or equal to CaO′ if CaO′ is less than Na_2O. CIA was calculated as:

$$CIA = \frac{Al_2O_3}{(Al_2O_3 + CaO^* + Na_2O + K_2O)}$$

2.2.4. Rock-Eval Analysis

In addition to samples analyzed on-board for total organic carbon (TOC) content (Figure 3; Planke et al., 2023), organic matter content for 112 samples from Hole U1568A were obtained with a Vinci Technologies Rock-Eval 6 device at the University of Oxford. Each sample was oven-dried at low temperature (<40°C) and powdered.

10.1029/2026PA005506

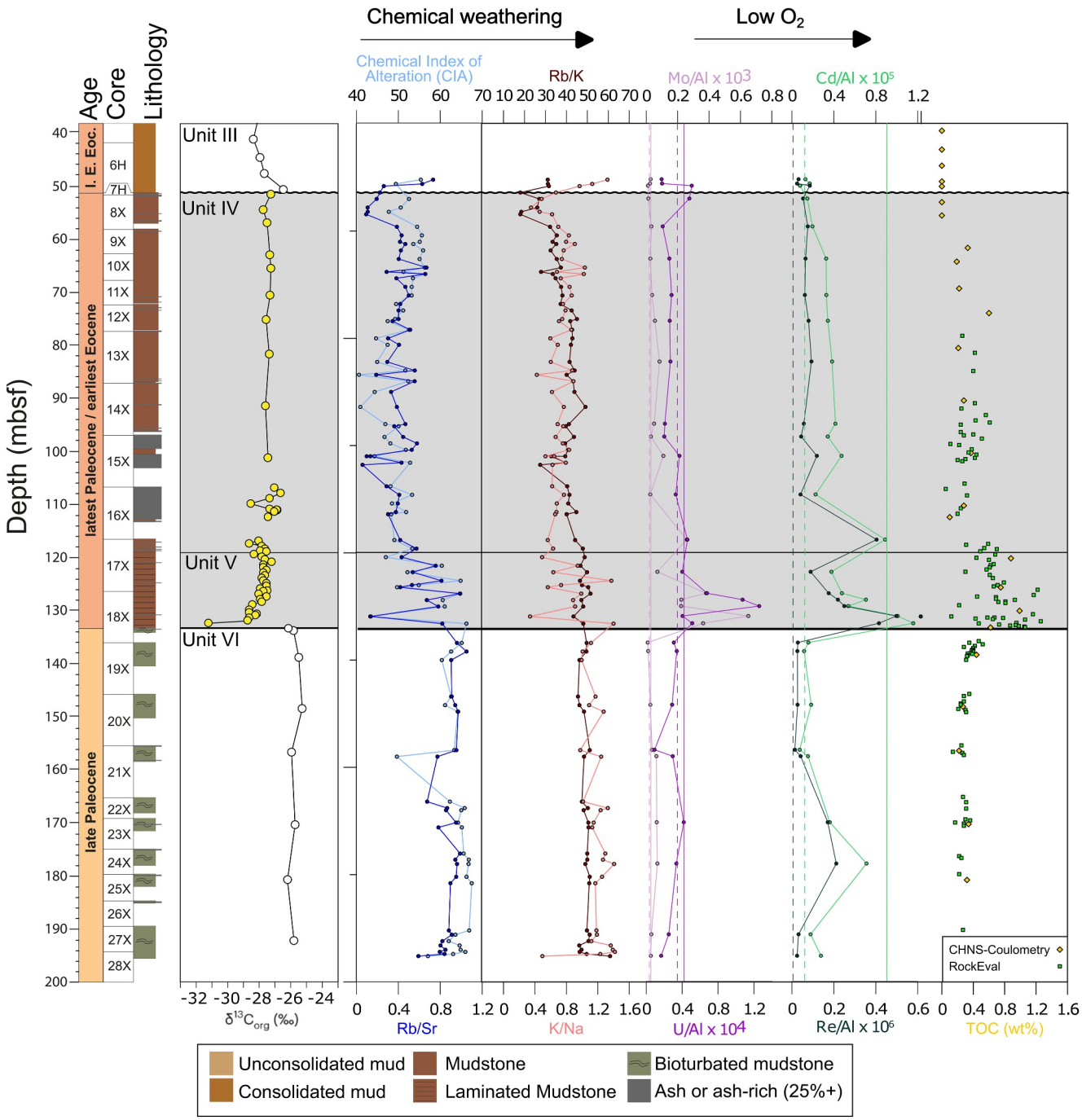

Figure 3. Variations in carbon isotopes, weathering intensity, redox conditions, and organic carbon content across the PETM (highlighted in grey) in Hole U1568A. Organic stable Carbon isotope ($\delta^{13}C_{org}$) data (Berndt et al., 2023; Vickers et al., 2024), weathering (Rb/Sr, CIA, K/Na, Rb/K) and redox proxies (U/Al, Mo/Al, Re/Al, Cd/Al), and TOC of core U1568A across the PETM interval (Planke et al., 2023).

Aliquots (50–120 mg) were weighed into steel crucibles and analyzed following standard procedures (Behar et al., 2001) to obtain TOC content. Reproducibility was estimated to be ±5% of the measured value or better with repeat analyses (n = 16) of an in-house standard (St Audries Bay shale with 2.7% TOC and ~50% carbonate).

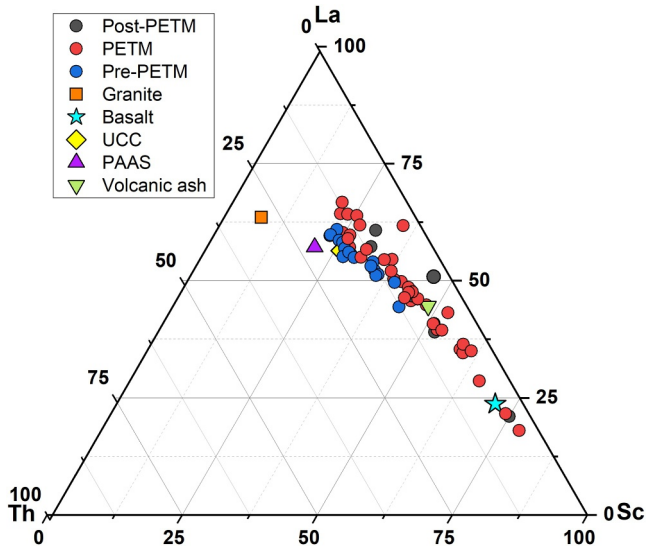

Figure 4. La-Th-Sc ternary plot (Jahn & Condie, 1995), showing provenance variations for IODP 396 Site. Blue, red, and black symbols represent pre-PETM, PETM, and post-PETM samples from Holes U1568A-B, U1567B, respectively. Compositions of, granite, basalt (Condie, 1993), upper continental crust (UCC), Post-Archean Australian Shale (PAAS) (Taylor & McLennan, 1985) and Volcanic ash (Baumann et al., 2024) are plotted for reference. The geochemical data indicate that all samples from pre-PETM, PETM and post-PETM generally show a mixed source that falls between the basalt and granite end member compositions.

3. Results

Paleoenvironmental changes across the pre-PETM, PETM, and post-PETM intervals were assessed using a suite of geochemical proxies (Figure 2. Weathering proxies indicate the highest values during the pre-PETM interval (26 samples), and lowest during the PETM (58 samples; Figure 3). Sediment provenance indicators (La, Th, and Sc) show considerable variability and overlapping distributions across all intervals, with no consistent stratigraphic separation between pre-PETM, PETM, and post-PETM samples (Figure 4). Redox- sensitive elements were normalized to Al to account for changes in the detrital component and associated dilution effects (Tribovillard et al., 2006). The ratios show interval-specific variations, with elevated values during the PETM and comparatively lower values in the pre- and post-PETM intervals (Figure 3). Provenance proxies include 19 pre-PETM, 40 PETM, and 6 post-PETM samples, while redox proxies include 9 pre-PETM, 18 PETM, and 2 post-PETM samples.

4. Discussion

The Vøring Basin is located within the NAIP and may therefore have been influenced by local volcanic activity, sediment heating, and associated hydrothermal processes (Berndt et al., 2023; Planke et al., 2023). These processes can modify bulk geochemical compositions through the input of volcanic material, sediment alteration, and redistribution of mobile elements, and may potentially overprint primary environmental signals (Y. Zhang et al., 2014). In addition, the hydrographically restricted nature of the basin may have contributed to enhanced local variability in sedimentary and geochemical records (Jones et al., 2023; Sømme et al., 2026). These factors need to be considered when interpreting geochemical proxies in this setting. Nevertheless, these records remain valuable for reconstructing environmental change, particularly when evaluated in a comparative and multi-proxy framework (Y. Zhang et al., 2014). Accordingly, we integrate weathering indicators (CIA and elemental ratios), provenance-sensitive tracers (La–Th–Sc), and redox-sensitive trace metal enrichments (Mo, Re, U, Cd) to assess the coherence and robustness of the recorded signals. This approach allows us to distinguish consistent regional trends associated with PETM-driven environmental change from potential local overprinting effects, thereby providing a reliable basis for interpreting weathering and redox evolution.

4.1. Intensity of Weathering During the PETM

An increase in chemical weathering intensity during the PETM has been reconstructed across the globe (Gibson et al., 2000; Pogge von Strandmann et al., 2021; Tanaka et al., 2022) and is generally attributed to elevated atmospheric CO_2 levels, high temperatures, and an enhanced hydrological cycle (Walters et al., 2022). Chemical weathering predominates in humid climates and significantly influences the major and trace element composition of silicate rocks and sediments. That is, chemical weathering leads to the progressive loss of mobile alkali and alkaline earth elements (e.g., sodium (Na), calcium (Ca), potassium(K)) relative to immobile aluminum (Al), resulting in elevated CIA values (Middelburg et al., 1988; Nesbitt & Young, 1982). In addition to the CIA, elemental ratios such as Rb/Sr, Rb/K and K/Na (Figure 3) are used to assess the degree of chemical weathering. Na and Sr are preferentially removed from solid phase during chemical weathering, whilst Rb and K are retained in the resultant clay minerals (Sawyer, 1986). K is typically preserved in clay minerals during moderate weathering, but is gradually lost under intense weathering. In highly weathered samples, Rb is more readily retained in clay minerals than K due to its larger ionic radius (Nesbitt et al., 1980).

However, the CIA and related elemental ratios can be influenced by changes in sediment provenance (Nesbitt & Young, 1982). To evaluate this potential effect, we use La–Th–Sc ternary plot (Jahn & Condie, 1995), as these elements are relatively immobile during chemical weathering and diagenesis. La and Th are enriched in felsic rocks (granite), while Sc is enriched in mafic rocks (basalt), so changes in these elements reflect a shift in source (Taylor & McLennan, 1985). Provenance analysis using La-Th-Sc ternary diagram show no distinct clustering

between Pre-PETM and PETM samples, indicating contribution from two well-mixed sources with no evidence for systematic change in provenance at the PETM onset (Figure 4). This suggests that the variations in CIA values are controlled primarily by the intensity of silicate weathering in the study area. Higher values (80–100) indicate intense chemical weathering, whereas lower values (50–70) suggest that physical weathering dominated in the source area (Nesbitt & Young, 1984).

In contrast to these global patterns, the CIA values in Hole U1568A show a decrease from the early to the middle part of the PETM vent infill (Figure 3), indicating a shift toward relatively low chemical weathering intensity. Comparable trends are also observed in Figures S1 in Supporting Information S1 (U1568B), S2 (U1567B), S3 (U1567A), S4 (U1567C), although differences in age-control between sites may affect the exact alignment of feature. This trend is supported by elemental ratios: Rb/Sr, Rb/K and K/Na are generally higher in pre-PETM samples compared to the PETM, suggesting a relatively stronger chemical weathering intensity prior to the PETM. Overall, the CIA values and elemental ratios suggest that chemical weathering intensity was less pronounced during the PETM compared to the pre-PETM interval, although the magnitude and consistency of this signal vary between individual proxies.

The PETM interval (Units IV–V in Hole U1568A) identified based on both biostratigraphic constraints and the CIE (Berndt et al., 2023) has a thickness of 81.9 m (Planke et al., 2023), which corresponds to an accumulation rate of ∼315–356 m/Ma, calculated assuming a PETM duration of ∼230–260 ka, following the chronology of Murphy et al. (2010). Pre- and post-PETM sedimentation rates were not quantitatively determined due to limited age control outside the PETM interval. This thick interval suggests a markedly elevated sedimentary input into the basin during the PETM, which corresponds to low chemical weathering intensity. The shift in sediment delivery and weathering regime may correspond to a number of factors. Regional evidence from the mid-Norwegian margin indicates that transient uplift between 56.0 and 55.5 Ma steepened slopes and strengthened fluvial activity, followed by rapid subsidence and burial of an incised landscape (Conway-Jones & White, 2022; Hartley et al., 2011). Such uplift and increased runoff likely promoted strong erosional processes along the margin. Consistent with this, observations from the nearby Froan Basin show that uplift-driven steep slopes and seasonal runoff produced valley incision, erosional networks, and large mud-rich gravity flows (Sømme et al., 2023), similar conditions in the Vøring Basin likely enhanced sediment supply and physical erosion during the PETM. This interpretation is supported by palynological vegetation reconstructions from the same core transect, which reveal rapid collapse of mature forests, landscape destabilization, and increased physical disturbance which includes reoccurring episodes of flooding and wildfire, processes which amplified terrestrial surface exposure and physical erosion (Nelissen et al., 2026). The loss of plant cover would have exposed soils and regolith to rainfall and runoff, increasing susceptibility to physical erosion. The PETM interval, marked by a shift from predominantly marine organic matter in Unit VI (late Paleocene) to terrestrial-dominated compositions in Units IV–V (earliest Eocene), provides independent evidence for enhanced physical erosion and the increased delivery of land-derived material to the Vøring Basin during this hyperthermal event (Berndt et al., 2023; Planke et al., 2023). Although fresh volcanic ash was intermittently supplied to the basin during the PETM (Vickers et al., 2024), its contribution is insufficient to explain the overall weathering signal observed here.

Whereas global studies indicate strong chemical weathering during the PETM, lithium isotope data suggest this reflects an increased input of older, eroded material (Pogge von Strandmann et al., 2021; Wei et al., 2025) rather than coeval chemical weathering intensity. A similar variability is observed in North Atlantic basin records, where the Fur Formation (Stokke et al., 2021) shows an opposing CIA response, whereas a record from the North Sea (Mariani et al., 2024) exhibits a comparable decrease in CIA during the PETM. This highlight spatial variability in weathering signal across connected but hydrographically and tectonically distinct depositional settings within the North Atlantic realm (Figure 5), including the Norwegian margin record presented here, which likewise shows consistently low CIA values.

These low CIA values are consistent with rapid delivery of fresh, newly eroded material from nearby uplift and NAIP volcanism. This likely reflects the predominance of relatively un-weathered source rocks in the northeast North Atlantic at the time. Overall, these observations indicate that physical erosion, rather than chemical weathering intensity, was the primary control on sediment supply in the North Atlantic during the PETM.

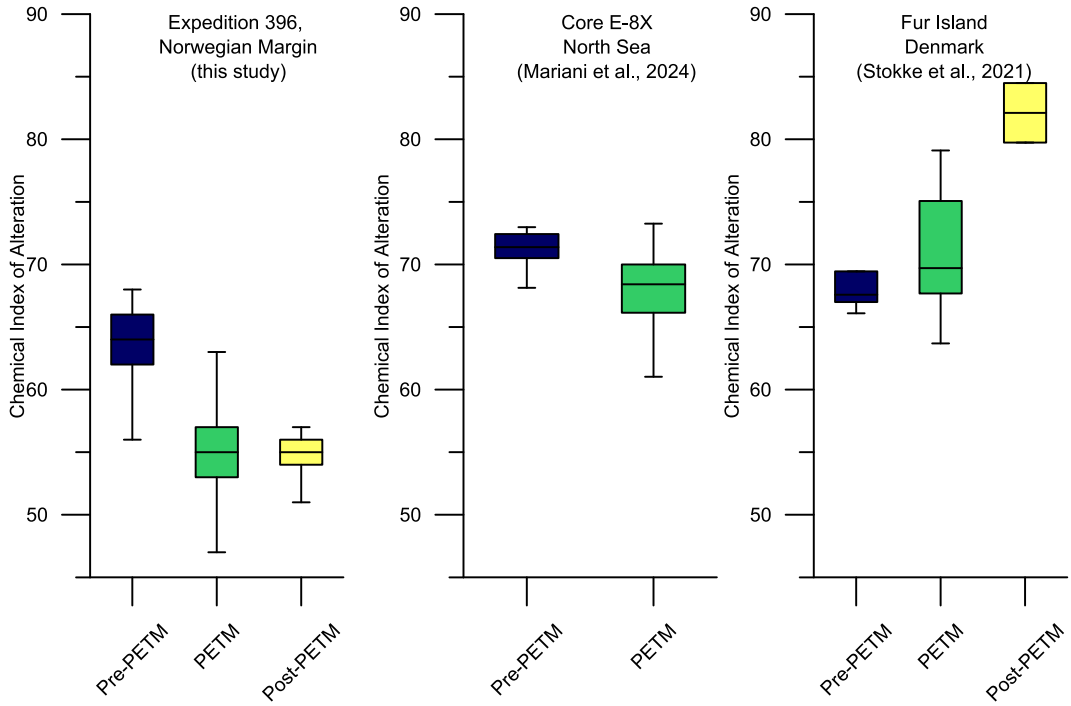

Figure 5. Comparison of Chemical Index of Alteration (CIA) values across pre-PETM, PETM, and post-PETM intervals from the Norwegian margin (this study), the North Sea Basin (Mariani et al., 2024), and the Fur Island in Denmark (Stokke et al., 2021). The solid black line in each box plot denotes the median. Boxes represent the interquartile range (25th–75th percentiles), with whiskers extending to 1.5 × IQR. Outliers beyond this range are not shown.

4.2. Redox Dynamics of the Vøring Basin During the PETM

The pronounced changes in continental weathering input during the PETM may have influenced redox conditions in the Vøring Basin. Against this backdrop, rapid PETM warming has been linked to changes in marine oxygen availability, with an increasing body of evidence suggesting a decline in global oceanic oxygen levels during this interval (Dickson et al., 2012). Many transition metals and redox-sensitive trace elements are valuable indicators of changing redox conditions in marine sediments, as they behave differently under oxic and anoxic conditions, allowing reconstruction of past environmental conditions (Calvert & Pedersen, 1993; Colodner et al., 1992; Crusius & Thomson, 2003). The oxyanions of U, Re, and Mo show conservative behavior in seawater. Additionally, U exists as insoluble U^{4+} (fluoride complex) in strongly reducing environments, leading to its accumulation in anoxic sediments, whereas under oxidizing conditions it is converted into soluble uranyl (U^{6+}) carbonate, thus causing anoxic sediments to contain higher uranium concentrations than oxic sediments (Wignall & Twitchett, 1996). Rhenium is enriched in mildly reducing (suboxic) sediments by diffusion from seawater. This process occurs at a redox potential that is marginally more reducing than that required for U, but prior to the reduction of Mo in strongly reducing, sulfidic sediments (Anbar et al., 1992; Crusius et al., 1996). The differing chemical behavior of Mo and U under similar reducing conditions provides insight into the extent of sulfide presence in anoxic water columns (Algeo & Tribovillard, 2009; Tossell, 2005). Unlike other redox-sensitive elements (e.g., U, Mo, Re), Cd has only one stable oxidation state (Cd^{2+}). In anoxic environments, even in the presence of micro quantities of free sulfide, Cd is effectively removed from the water through the formation of insoluble CdS (Rosenthal et al., 1995).

Evidence suggests that oxygen depletion during the PETM was spatially variable, with low oxygen levels in open ocean regions, while some continental shelves and enclosed basins–particularly across the Northern Hemisphere, including the Tethys, Peri-Tethys, North Sea, and Arctic–developed fully anoxic or sulfidic conditions during this interval (Behrooz et al., 2024; Clarkson et al., 2021; Dickson et al., 2012; Pälike et al., 2014; Sluijs et al., 2014). Biomarker studies further reveal that euxinic conditions, characterized by the presence of free hydrogen sulfide in the water column, extended into the photic zone in several regions, including the Arctic Ocean, the Gulf Coastal Plains (Sluijs et al., 2014), the equatorial Atlantic (Frieling et al., 2017), the eastern North Sea (Schoon

et al., 2015), the West Siberian Sea (Frieling et al., 2014), and the North Central Peri-Tethys (Behrooz et al., 2024).

Consistent with this evidence, our results indicate marked increases in Mo/Al, Re/Al, U/Al, and Cd/Al at the Unit VI–V boundary, reflecting intensifying anoxia and the development of more reducing, sulfidic conditions. At Hole U1568A, the stratigraphic interval corresponding to the PETM onset is incompletely preserved, limiting the resolution of redox changes relative to the onset of CIE. Redox sensitive proxies are available for Holes U1568A, U1568B and U1567B; thus, relative temporal relationships can be assessed across these three records. In U1568A, the increase broadly coincides with the PETM onset (Figure 3), whereas in U1568B (Figure S1 in Supporting Information S1) the main redox transition occurs just prior to unit boundary (VI-V) than the exact onset of the CIE. In U1567B (Figure S2 in Supporting Information S1), redox proxy increases are recorded within the vent-infill succession corresponding to the PETM onset interval. Taken together, the records indicate a rapid development of reducing conditions during the early PETM, although the precise timing relative to the CIE remains uncertain owing to variable stratigraphic resolution across the boundary. These observations indicate that redox changes were influenced both by PETM-driven environmental shifts and by pre-existing conditions, a pattern also reflected in the weathering data across the unit boundary. It should be noted that redox-sensitive trace metal enrichments may reflect not only changes in oxygenation but also variations in external metal supply such as ash fall (K. Zhang et al., 2025), sedimentation rate, and local environmental and post-depositional processes. In hydrographically restricted continental margin settings like the Vøring Basin (Jones et al., 2023) their concentrations and preservation can additionally be influenced by particulate shuttle effects and basin restriction, resulting in highly variable enrichments that may not fully capture the extent of sulfidic conditions, in contrast to the more consistent signals observed in open-ocean environments (Algeo & Li, 2020; Algeo & Lyons, 2006; Algeo & Rowe, 2012; Bennett & Canfield, 2020; Hoogakker et al., 2025; Sweere et al., 2016). In restricted basins even relatively, small variations in local circulation strength or seawater temperature may further influence oxygen availability (Rakshit et al., 2023).

Redox sensitive element/Al ratios continue to rise from the onset until the middle of the syn-PETM vent infill (Unit V), peaking before gradually declining towards levels comparable to the pre-PETM strata in Unit IV (Figure 3). However, as the onset of the PETM interval may not be preserved (Berndt et al., 2023), it is unclear whether this represents the actual middle of the PETM. The geochemical and sedimentological evidence from the Vøring Basin indicates that deoxygenation was established during the earliest PETM, as supported by laminated, non-bioturbated sediments and presence of tiny pyrite framboids (<20 μm) in Unit V (cores U1568A-B, U1567 A-C) (Planke et al., 2023), suggesting that the water column near the seabed became anoxic with possible development of sulfidic conditions in the sediment pore waters. This aligns with global patterns of oceanic anoxia including those in the North Sea (Mariani et al., 2024), South Atlantic (Chang et al., 2018), and the Bay of Biscay in the eastern North Atlantic (Clarkson et al., 2021), which also experienced reducing conditions during the earliest part of the PETM. U/Al and Re/Al ratios reveal that after the initial deoxygenation during the early PETM, the middle portion of the vent infill returned to more oxic conditions. This pattern may reflect a combination of factors, including the extremely shallow nature of the Vøring margin IODP Sites (~30–50 m water depth during the PETM (Berndt et al., 2023; Planke et al., 2023)) and the high-resolution sampling that could capture short-lived oxic intervals not recorded at many other sites. Toward the top of the syn-PETM vent infill, however, U/Al and Re/Al display a secondary increase, indicating renewed oxygen depletion and the development of possible suboxic conditions. In contrast, Mo/Al, Cd/AL do not show corresponding enrichments, suggesting that fully euxinic conditions were not reached (Figure 3). These observations highlight that deoxygenation during the PETM was dynamic and spatially variable: unlike basins with persistent anoxia or euxinia, the Vøring Basin experienced oscillating redox conditions.

4.3. Drivers of Regional Euxinia in the Vøring Basin During the PETM

Previous studies suggest that the rapid onset of regional euxinia at the PETM was driven by multiple interrelated factors including rising temperatures, enhanced continental nutrient inputs, restricted basin circulation, elevated primary productivity, intensified oxygen consumption during organic matter degradation and methane oxidation (Clarkson et al., 2021; Dickson et al., 2014; Remmelzwaal et al., 2019). Ongoing extensional tectonics along plate boundaries likely enhanced nutrient delivery to surface waters (Gernon et al., 2016). Plume-based rifting likely amplified this enrichment through uplift-driven erosion, hydrothermal activity, and volcanic ash deposition, stimulating microbial and phytoplankton growth and triggering large-scale blooms that influenced

biogeochemical and evolutionary cycles. In tectonically restricted basins like the Norwegian Sea, even minor uplift and/or hydroclimatic changes could strongly amplify nutrient availability and primary productivity (Mariani et al., 2024).

Diatoms, which represent the major group of phytoplankton in the PETM succession of our cores (Planke et al., 2023) can efficiently utilize iron (Fe) from volcanic sources (Duggen et al., 2007). Sediment deposits resulting from intense physical weathering provide bioavailable Fe from primary minerals (Shoenfelt et al., 2019), while volcanic ash deposition enhances nutrient availability through dissolution of adsorbed metal salts and aerosols (Jones & Gislason, 2008; Longman, Mills, et al., 2021; Longman et al., 2022). Bioassay experiments show that phytoplankton growth is maximized when multiple nutrients are available simultaneously rather than a single limiting element (Mills et al., 2004). Basaltic terrains, although covering only ∼4.6% of the continental surface, contribute 30%–35% of the terrestrial silicate weathering flux due to their high reactivity (Dessert et al., 2003). Due to ongoing emplacement of the NAIP, the continents surrounding the Vøring Basin would have been comprised primarily of basalt, thereby providing a source of reactive material to the basin under enhanced physical erosion conditions during the PETM. Although the CIA data (Figure 3) suggest low overall chemical weathering intensity, enhanced physical erosion during the PETM likely increased the delivery of fresh basaltic material, where rapid or localized water rock interactions could still facilitate nutrient release without requiring sustained high-intensity chemical weathering (Jenckes et al., 2024). Indeed, the supply of unweathered, and therefore reactive phase-rich material may act to enhance the amount of nutrients leached as they enter the marine realm (Struve et al., 2026). As a result, nutrient availability in the basin was likely high, leading to elevated productivity, evidenced by the high diatom accumulation rates during the PETM (Planke et al., 2023).

Total organic carbon (TOC) concentrations (Figure 3) reported from Core U1568A (Planke et al., 2023) increase coincident with the onset of the PETM. However, without well-constrained mass accumulation rates, it is difficult to determine whether this increase reflects enhanced organic carbon preservation or variations in sediment dilution. Interpretation is further complicated by the unconformable Unit VI–V boundary at Site U1568A and the relatively thin interval separating the latest Paleocene strata from the PETM succession, which introduces uncertainty in the precise stratigraphic placement of these changes. Enhanced sedimentation rates, likely driven by intensified continental weathering and erosion under a more active hydrological cycle, acted as key negative feedback on the CIE and associated warming by promoting carbon burial (John et al., 2008).

The thickest and most abundant ash layers in Core U1568A occur between ∼70 and ∼110 mbsf (Vickers et al., 2024), reflecting enhanced local ash deposition within the middle portion of the vent-infill PETM succession. In the earlier PETM interval (∼133–110 mbsf), ash layers are either very thin or largely reworked, making their contribution to nutrient supply more limited. Elevated productivity during this interval was likely supported primarily by nutrients released through intensified physical weathering and erosion of freshly emplaced igneous rocks, with possible minor contributions from the thin or reworked volcanic material.

Productivity interpretations are primarily informed by the exceptionally preserved diatom record from site U1567, where laminated diatomites and high diatom abundances indicate elevated biogenic productivity (Nelissen et al., 2026; Planke et al., 2023). In contrast, the utility of vent-proximal Site U1568A for reconstructing productivity is limited, as its biosiliceous record is compromised by silica diagenesis and alteration within the thicker, ash rich vent-infill succession. Conventional productivity proxies (e.g., Ba/Al and P/Al) are not considered reliable in this interval due to strong dilution by volcanic and detrital inputs and potential post-depositional redistribution under variable redox conditions, where P can be remobilized and Ba may be affected by barite dissolution under sulfate-reducing conditions (Tribovillard et al., 2006).

Overall, nutrient availability throughout the PETM interval was likely maintained by multiple sources—including enhanced physical erosion of basalt-rich catchments and inputs from volcanic ash—which together fuelled the high primary productivity, as reflected in diatom rich sediments and blooms in Units IV and V of the PETM vent infill succession (Planke et al., 2023). The resulting surge in productivity and organic matter remineralization is potentially one of the primary mechanisms leading to the establishment of euxinia during the early PETM, a pattern that is consistent with observations from the North Sea (Mariani et al., 2024). Towards the top of the PETM vent infill, the Vøring Basin returned to suboxic conditions (Figure 3). Although oxygen depletion was less intense than in the early PETM euxinia, the underlying mechanism was likely similar, with nutrient-rich, minimally leached material delivered through physical erosion stimulating productivity and enhancing organic matter degradation in the basin.

Fluctuations in primary productivity, in addition to promoting euxinic conditions, can strongly influence atmospheric CO_2 levels and thus climate over geological timescales (Falkowski et al., 1998). At the Paleocene-Eocene boundary, elevated primary productivity and associated organic carbon burial acted as a local carbon sink drawing down atmospheric CO_2 (Kaya et al., 2022; Papadomanolaki et al., 2022). Low-oxygen (anoxic) conditions likely facilitated more efficient carbon burial in coastal and nearshore environments, with some high-latitude regions likely acting as sites of additional carbon storage during portions of the ~200 kyr interval represented by the CIE (Wieczorek et al., 2013). Marginal and epicontinental seas—including the North Sea and nearby basins—probably functioned as important carbon sinks (Kaya et al., 2022), with additional burial during the early recovery phase further contributing to carbon sequestration. The interplay between fluctuations in nutrient input, productivity, oxygen levels, run-off and high sedimentation rates regulated carbon sequestration in the eastern North Atlantic, contributing to the PETM recovery.

5. Conclusion

Our study demonstrates that physical erosion, rather than chemical weathering, played the primary role in controlling nutrient fluxes to the Vøring Basin during the PETM. Pulses of enhanced sediment input fueled high primary productivity and triggered transient anoxic-euxinic conditions, limited to the onset of the event and largely subsiding by the middle of the PETM vent infill. These findings highlight the mechanistic role of sediment dynamics in shaping carbon burial and ocean biogeochemistry under rapid warming, providing a clearer understanding of how continental processes influence marine responses during extreme greenhouse climates. Future work integrating additional proxy records and regional comparisons will help constrain the spatial variability and global relevance of these processes.

Conflict of Interest

The authors declare no conflicts of interest relevant to this study.

Availability Statement

All data supporting the findings of this study are publicly available and have been archived in Figshare (Sandhya et al., 2026).

Acknowledgments

We gratefully acknowledge financial support from the German Research Foundation (DFG) through the grant awarded to Jack Longman (Grant 507196996). JF acknowledges funding from the UK IODP Grant NE/W007142/1 for the Rock-Eval analysis. MTJ is supported by the PETROMAKS program from The Research Council of Norway, with the RCN project number 336293 (PALMAR). We thank Eleonore Gründken and Martina Schulz for their invaluable technical assistance. We are also grateful to Dr. Frederik Gäng and Dr. Philipp Böning for their support with quality control of the data. We also thank Andre Bersen for his assistance with XRF sample preparation. Finally, we thank the Science Party, Captain, and crew of IODP Expedition 396 for their dedicated efforts in collecting the samples that made this study possible. We thank two anonymous reviewers for their very constructive advice that significantly improved the manuscript. Open Access funding enabled and organized by Projekt DEAL.

References

Algeo, T. J., & Li, C. (2020). Redox classification and calibration of redox thresholds in sedimentary systems. *Geochimica et Cosmochimica Acta*, *287*, 8–26. https://doi.org/10.1016/j.gca.2020.01.055

Algeo, T. J., & Lyons, T. W. (2006). Mo–total organic carbon covariation in modern anoxic marine environments: Implications for analysis of paleoredox and paleohydrographic conditions. *Paleoceanography*, *21*(1), 2004PA001112. https://doi.org/10.1029/2004PA001112

Algeo, T. J., & Rowe, H. (2012). Paleoceanographic applications of trace-metal concentration data. *Chemical Geology*, *324–325*, 6–18. https://doi.org/10.1016/j.chemgeo.2011.09.002

Algeo, T. J., & Tribovillard, N. (2009). Environmental analysis of paleoceanographic systems based on molybdenum–uranium covariation. *Chemical Geology*, *268*(3–4), 211–225. https://doi.org/10.1016/j.chemgeo.2009.09.001

Anbar, A. D., Creaser, R. A., Papanastassiou, D. A., & Wasserburg, G. J. (1992). Rhenium in seawater: Confirmation of generally conservative behavior. *Geochimica et Cosmochimica Acta*, *56*(11), 4099–4103. https://doi.org/10.1016/0016-7037(92)90021-A

Baumann, N. B., Regelous, M., Adatte, T., Thibault, N. R., Regelous, A., Schultz, B. P., et al. (2024). Linking the PETM and North Atlantic volcanism using tellurium in sediments. *Palaeogeography, Palaeoclimatology, Palaeoecology*, *656*, 112575. https://doi.org/10.1016/j.palaeo.2024.112575

Behar, F., Beaumont, V., De, B., & Penteado, H. L. (2001). Rock-Eval 6 technology: Performances and developments. *Oil and Gas Science and Technology*, *56*(2), 111–134. https://doi.org/10.2516/ogst:2001013

Behrooz, L., Monteiro, F. M., Naafs, B. D. A., Taylor, K. W. R., Dickson, A. J., Graham, O. A., et al. (2024). North-East Peri-Tethyan water column deoxygenation and Euxinia at the Paleocene Eocene thermal maximum. *Paleoceanography and Paleoclimatology*, *39*(11), e2023PA004828. https://doi.org/10.1029/2023PA004828

Bennett, W. W., & Canfield, D. E. (2020). Redox-sensitive trace metals as paleoredox proxies: A review and analysis of data from modern sediments. *Earth-Science Reviews*, *204*, 103175. https://doi.org/10.1016/j.earscirev.2020.103175

Berndt, C., Planke, S., Alvarez Zarikian, C. A., Frieling, J., Jones, M. T., Millett, J. M., et al. (2023). Shallow-water hydrothermal venting linked to the Palaeocene–Eocene thermal maximum. *Nature Geoscience*, *16*(9), 803–809. https://doi.org/10.1038/s41561-023-01246-8

Bolle, M.-P., & Adatte, T. (2001). Palaeocene-early Eocene climatic evolution in the Tethyan realm: Clay mineral evidence. *Clay Minerals*, *36*(2), 249–261. https://doi.org/10.1180/000985501750177979

Böning, P., Brumsack, H.-J., Böttcher, M. E., Schnetger, B., Kriete, C., Kallmeyer, J., & Borchers, S. L. (2004). Geochemistry of Peruvian near-surface sediments. *Geochimica et Cosmochimica Acta*, *68*(21), 4429–4451. https://doi.org/10.1016/j.gca.2004.04.027

Calvert, S. E., & Pedersen, T. F. (1993). Geochemistry of Recent oxic and anoxic marine sediments: Implications for the geological record. *Marine Geology*, *113*(1–2), 67–88. https://doi.org/10.1016/0025-3227(93)90150-T

Carmichael, M. J., Inglis, G. N., Badger, M. P. S., Naafs, B. D. A., Behrooz, L., Remmelzwaal, S., et al. (2017). Hydrological and associated biogeochemical consequences of rapid global warming during the Paleocene-Eocene thermal maximum. *Global and Planetary Change*, *157*, 114–138. https://doi.org/10.1016/j.gloplacha.2017.07.014

Chang, L., Harrison, R. J., Zeng, F., Berndt, T. A., Roberts, A. P., Heslop, D., & Zhao, X. (2018). Coupled microbial bloom and oxygenation decline recorded by magnetofossils during the Palaeocene–Eocene thermal maximum. *Nature Communications*, *9*(1), 4007. https://doi.org/10.1038/s41467-018-06472-y

Charles, A. J., Condon, D. J., Harding, I. C., Pälike, H., Marshall, J. E. A., Cui, Y., et al. (2011). Constraints on the numerical age of the Paleocene-Eocene boundary: Age of the P-E boundary. *Geochemistry, Geophysics, Geosystems*, *12*(6). https://doi.org/10.1029/2010GC003426

Chen, Z., Ding, Z., Yang, S., Zhang, C., & Wang, X. (2016). Increased precipitation and weathering across the Paleocene-Eocene thermal maximum in central China. *Geochemistry, Geophysics, Geosystems*, *17*(6), 2286–2297. https://doi.org/10.1002/2016GC006333

Clarkson, M. O., Lenton, T. M., Andersen, M. B., Bagard, M.-L., Dickson, A. J., & Vance, D. (2021). Upper limits on the extent of seafloor anoxia during the PETM from uranium isotopes. *Nature Communications*, *12*(1), 399. https://doi.org/10.1038/s41467-020-20486-5

Cohen, A. S., & Coe, A. L. (2012). Seawater oxygenation during the Paleocene-Eocene thermal maximum. *Geology*, *40*(7), 639–642. https://doi.org/10.1130/G32977.1

Colodner, D. C., Boyle, E. A., Edmond, J. M., & Thomson, J. (1992). Post-depositional mobility of platinum, iridium and rhenium in marine sediments. *Nature*, *358*(6385), 402–404. https://doi.org/10.1038/358402a0

Condie, K. C. (1993). Chemical composition and evolution of the upper continental crust: Contrasting results from surface samples and shales. *Chemical Geology*, *104*(1–4), 1–37. https://doi.org/10.1016/0009-2541(93)90140-E

Conway-Jones, B. W., & White, N. (2022). Paleogene buried landscapes and climatic aberrations triggered by mantle plume activity. *Earth and Planetary Science Letters*, *593*, 117644. https://doi.org/10.1016/j.epsl.2022.117644

Crusius, J., Calve, S., Pedersen, T., & Sage, D. (1996). Rhenium and molybdenum enrichments in sediments as indicators of oxic, suboxic and sulfidic conditions of deposition.

Crusius, J., & Thomson, J. (2003). Mobility of authigenic rhenium, silver, and selenium during postdepositional oxidation in marine sediments. *Geochimica et Cosmochimica Acta*, *67*(2), 265–273. https://doi.org/10.1016/S0016-7037(02)01075-X

Dessert, C., Dupré, B., Gaillardet, J., François, L. M., & Allègre, C. J. (2003). Basalt weathering laws and the impact of basalt weathering on the global carbon cycle. *Chemical Geology*, *202*(3–4), 257–273. https://doi.org/10.1016/j.chemgeo.2002.10.001

Dickson, A. J., Cohen, A. S., & Coe, A. L. (2012). Seawater oxygenation during the Paleocene-Eocene thermal maximum. *Geology*, *40*(7), 639–642. https://doi.org/10.1130/G32977.1

Dickson, A. J., Rees-Owen, R. L., März, C., Coe, A. L., Cohen, A. S., Pancost, R. D., et al. (2014). The spread of marine anoxia on the northern Tethys margin during the Paleocene-Eocene thermal maximum: Tethys redox during the PETM. *Paleoceanography*, *29*(6), 471–488. https://doi.org/10.1002/2014PA002629

Duggen, S., Croot, P., Schacht, U., & Hoffmann, L. (2007). Subduction zone volcanic ash can fertilize the surface ocean and stimulate phytoplankton growth: Evidence from biogeochemical experiments and satellite data. *Geophysical Research Letters*, *34*(1), 2006GL027522. https://doi.org/10.1029/2006GL027522

Dunkley Jones, T., Lunt, D. J., Schmidt, D. N., Ridgwell, A., Sluijs, A., Valdes, P. J., & Maslin, M. (2013). Climate model and proxy data constraints on ocean warming across the Paleocene–Eocene thermal maximum. *Earth-Science Reviews*, *125*, 123–145. https://doi.org/10.1016/j.earscirev.2013.07.004

Falkowski, P. G., Barber, R. T., & Smetacek, V. (1998). Biogeochemical controls and feedbacks on ocean primary production. *Science*, *281*(5374), 200–206. https://doi.org/10.1126/science.281.5374.200

Fedo, C. M., Wayne Nesbitt, H., & Young, G. M. (1995). Unraveling the effects of potassium metasomatism in sedimentary rocks and paleosols, with implications for paleoweathering conditions and provenance. *Geology*, *23*(10), 921. https://doi.org/10.1130/0091-7613(1995)023<0921:UTEOPM>2.3.CO;2

Frieling, J., Gebhardt, H., Huber, M., Adekeye, O. A., Akande, S. O., Reichart, G.-J., et al. (2017). Extreme warmth and heat-stressed plankton in the tropics during the Paleocene-Eocene thermal maximum. *Science Advances*, *3*(3), e1600891. https://doi.org/10.1126/sciadv.1600891

Frieling, J., Iakovleva, A. I., Reichart, G.-J., Aleksandrova, G. N., Gnibidenko, Z. N., Schouten, S., & Sluijs, A. (2014). Paleocene–Eocene warming and biotic response in the epicontinental West Siberian Sea. *Geology*, *42*(9), 767–770. https://doi.org/10.1130/G35724.1

Frieling, J., Svensen, H. H., Planke, S., Cramwinckel, M. J., Selnes, H., & Sluijs, A. (2016). Thermogenic methane release as a cause for the long duration of the PETM. *Proceedings of the National Academy of Sciences*, *113*(43), 12059–12064. https://doi.org/10.1073/pnas.1603348113

Gernon, T. M., Hincks, T. K., Tyrrell, T., Rohling, E. J., & Palmer, M. R. (2016). Snowball Earth ocean chemistry driven by extensive ridge volcanism during Rodinia breakup. *Nature Geoscience*, *9*(3), 242–248. https://doi.org/10.1038/ngeo2632

Gibson, T. G., Bybell, L. M., & Mason, D. B. (2000). Stratigraphic and climatic implications of clay mineral changes around the Paleocene/Eocene boundary of the northeastern US margin. *Sedimentary Geology*, *134*(1–2), 65–92. https://doi.org/10.1016/S0037-0738(00)00014-2

Handley, L., O'Halloran, A., Pearson, P. N., Hawkins, E., Nicholas, C. J., Schouten, S., et al. (2012). Changes in the hydrological cycle in tropical East Africa during the Paleocene–Eocene thermal maximum. *Palaeogeography, Palaeoclimatology, Palaeoecology*, *329–330*, 10–21. https://doi.org/10.1016/j.palaeo.2012.02.002

Hartley, R. A., Roberts, G. G., White, N., & Richardson, C. (2011). Transient convective uplift of an ancient buried landscape. *Nature Geoscience*, *4*(8), 562–565. https://doi.org/10.1038/ngeo1191

Hoogakker, B. A. A., Davis, C., Wang, Y., Kusch, S., Nilsson-Kerr, K., Hardisty, D. S., et al. (2025). Reviews and syntheses: Review of proxies for low-oxygen paleoceanographic reconstructions. *Biogeosciences*, *22*(4), 863–957. https://doi.org/10.5194/bg-22-863-2025

Jahn, B.-M., & Condie, K. C. (1995). Evolution of the Kaapvaal Craton as viewed from geochemical and Sm-Nd isotopic analyses of intracratonic pelites. *Geochimica et Cosmochimica Acta*, *59*(11), 2239–2258. https://doi.org/10.1016/0016-7037(95)00103-7

Jenckes, J., Muñoz, S., Ibarra, D. E., Boutt, D. F., & Munk, L. A. (2024). Geochemical weathering variability in high latitude watersheds of the Gulf of Alaska. *Journal of Geophysical Research: Earth Surface*, *129*(3), e2023JF007284. https://doi.org/10.1029/2023JF007284

John, C. M., Banerjee, N. R., Longstaffe, F. J., Sica, C., Law, K. R., & Zachos, J. C. (2012). Clay assemblage and oxygen isotopic constraints on the weathering response to the Paleocene-Eocene thermal maximum, east coast of North America. *Geology*, *40*(7), 591–594. https://doi.org/10.1130/G32785.1

John, C. M., Bohaty, S. M., Zachos, J. C., Sluijs, A., Gibbs, S., Brinkhuis, H., & Bralower, T. J. (2008). North American continental margin records of the Paleocene-Eocene thermal maximum: Implications for global carbon and hydrological cycling. *Paleoceanography*, *23*(2), 2007PA001465. https://doi.org/10.1029/2007PA001465

Jones, M. T., Augland, L. E., Ovtcharova, M., Stokke, E. W., Ganerød, M., & Planke, S. (2025). New constraints on the absolute age and duration of the Paleocene – Eocene Thermal maximum (PETM) from ash layer +19 in Denmark. *Earth and Planetary Science Letters*, *671*, 119643. https://doi.org/10.1016/j.epsl.2025.119643

Jones, M. T., & Gislason, S. R. (2008). Rapid releases of metal salts and nutrients following the deposition of volcanic ash into aqueous environments. *Geochimica et Cosmochimica Acta*, *72*(15), 3661–3680. https://doi.org/10.1016/j.gca.2008.05.030

Jones, M. T., Percival, L. M. E., Stokke, E. W., Frieling, J., Mather, T. A., Riber, L., et al. (2019). Mercury anomalies across the Palaeocene–Eocene thermal maximum. *Climate of the Past*, *15*(1), 217–236. https://doi.org/10.5194/cp-15-217-2019

Jones, M. T., Stokke, E. W., Rooney, A. D., Frieling, J., Pogge Von Strandmann, P. A. E., Wilson, D. J., et al. (2023). Tracing North Atlantic volcanism and seaway connectivity across the Paleocene–Eocene thermal maximum (PETM). *Climate of the Past*, *19*(8), 1623–1652. https://doi.org/10.5194/cp-19-1623-2023

Kaya, M. Y., Dupont-Nivet, G., Frieling, J., Fioroni, C., Rohrmann, A., Altıner, S. Ö., et al. (2022). The Eurasian Epicontinental Sea was an important carbon sink during the Palaeocene-Eocene thermal maximum. *Communications Earth & Environment*, *3*(1), 124. https://doi.org/10.1038/s43247-022-00451-4

Knox, R. W. O. (1984). Nannoplankton zonation and the Palaeocene/Eocene boundary beds of NW Europe: An indirect correlation by means of volcanic ash layers. *Journal of the Geological Society*, *141*(6), 993–999. https://doi.org/10.1144/gsjgs.141.6.0993

Korasidis, V. A., Wing, S. L., Shields, C. A., & Kiehl, J. T. (2022). Global changes in terrestrial vegetation and Continental climate during the Paleocene-Eocene thermal maximum. *Paleoceanography and Paleoclimatology*, *37*(4), e2021PA004325. https://doi.org/10.1029/2021PA004325

Longman, J., Gernon, T. M., Palmer, M. R., Jones, M. T., Stokke, E. W., & Svensen, H. H. (2021). Marine diagenesis of tephra aided the Palaeocene-Eocene thermal maximum termination. *Earth and Planetary Science Letters*, *571*, 117101. https://doi.org/10.1016/j.epsl.2021.117101

Longman, J., Mills, B. J. W., Manners, H. R., Gernon, T. M., & Palmer, M. R. (2021). Late Ordovician climate change and extinctions driven by elevated volcanic nutrient supply. *Nature Geoscience*, *14*(12), 924–929. https://doi.org/10.1038/s41561-021-00855-5

Longman, J., Palmer, M. R., Gernon, T. M., Manners, H. R., & Jones, M. T. (2022). Subaerial volcanism is a potentially major contributor to oceanic iron and manganese cycles. *Communications Earth & Environment*, *3*(1), 60. https://doi.org/10.1038/s43247-022-00389-7

Mariani, E., Kender, S., Hesselbo, S. P., Bogus, K., Littler, K., Riding, J. B., et al. (2024). Large igneous province control on ocean anoxia and eutrophication in the North Sea at the Paleocene–Eocene thermal maximum. *Paleoceanography and Paleoclimatology*, *39*(4), e2023PA004756. https://doi.org/10.1029/2023PA004756

McInerney, F. A., & Wing, S. L. (2011). The Paleocene-Eocene thermal maximum: A perturbation of carbon cycle, climate, and biosphere with implications for the future. *Annual Review of Earth and Planetary Sciences*, *39*(1), 489–516. https://doi.org/10.1146/annurev-earth-040610-133431

McLennan, S. M., Hemming, S., McDaniel, D. K., & Hanson, G. N. (1993). Geochemical approaches to sedimentation, provenance, and tectonics. In *Geological society of America special papers* (Vol. 284, pp. 21–40). Geological Society of America. https://doi.org/10.1130/SPE284-p21

Middelburg, J. J., Van Der Weijden, C. H., & Woittiez, J. R. W. (1988). Chemical processes affecting the mobility of major, minor and trace elements during weathering of granitic rocks. *Chemical Geology*, *68*(3–4), 253–273. https://doi.org/10.1016/0009-2541(88)90025-3

Mills, M. M., Ridame, C., Davey, M., La Roche, J., & Geider, R. J. (2004). Iron and phosphorus co-limit nitrogen fixation in the eastern tropical North Atlantic. *Nature*, *429*(6989), 292–294. https://doi.org/10.1038/nature02550

Murphy, B. H., Farley, K. A., & Zachos, J. C. (2010). An extraterrestrial 3He-based timescale for the Paleocene–Eocene thermal maximum (PETM) from Walvis Ridge, IODP site 1266. *Geochimica et Cosmochimica Acta*, *74*(17), 5098–5108. https://doi.org/10.1016/j.gca.2010.03.039

Nelissen, M., Willard, D. A., Van Konijnenburg-van Cittert, H., Bowen, G. J., Hollaar, T., Sluijs, A., et al. (2026). Widespread terrestrial ecosystem disruption at the onset of the Paleocene–Eocene thermal maximum. *Proceedings of the National Academy of Sciences*, *123*(4), e2509231122. https://doi.org/10.1073/pnas.2509231122

Nesbitt, H. W., Markovics, G., & Price, R. C. (1980). Chemical processes affecting alkalis and alkaline earths during continental weathering. *Geochimica et Cosmochimica Acta*, *44*(11), 1659–1666. https://doi.org/10.1016/0016-7037(80)90218-5

Nesbitt, H. W., & Young, G. M. (1982). Early Proterozoic climates and plate motions inferred from major element chemistry of lutites. *Nature*, *299*(5885), 715–717. https://doi.org/10.1038/299715a0

Nesbitt, H. W., & Young, G. M. (1984). Prediction of some weathering trends of plutonic and volcanic rocks based on thermodynamic and kinetic considerations. *Geochimica et Cosmochimica Acta*, *48*(7), 1523–1534. https://doi.org/10.1016/0016-7037(84)90408-3

Pälike, C., Delaney, M. L., & Zachos, J. C. (2014). Deep-sea redox across the Paleocene-Eocene thermal maximum. *Geochemistry, Geophysics, Geosystems*, *15*(4), 1038–1053. https://doi.org/10.1002/2013GC005074

Papadomanolaki, N. M., Sluijs, A., & Slomp, C. P. (2022). Eutrophication and deoxygenation forcing of marginal marine organic carbon burial during the PETM. *Paleoceanography and Paleoclimatology*, *37*(3), e2021PA004232. https://doi.org/10.1029/2021PA004232

Penman, D. E., Keller, A., D'haenens, S., Kirtland Turner, S., & Hull, P. M. (2019). Atlantic deep-sea cherts associated with Eocene hyperthermal events. *Paleoceanography and Paleoclimatology*, *34*(2), 287–299. https://doi.org/10.1029/2018PA003503

Piedrahita, V. A., Heslop, D., Roberts, A. P., Rohling, E. J., Galeotti, S., Florindo, F., & Li, J. (2025). Assessing the duration of the Paleocene-Eocene thermal maximum. *Geophysical Research Letters*, *52*(7), e2024GL113117. https://doi.org/10.1029/2024GL113117

Planke, S., Berndt, C., & Alvarez Zarikian, C. A., & Expedition 396 Scientists. (2023). Mid-Norwegian margin magmatism and paleoclimate implications. *International Ocean Discovery Program*. https://doi.org/10.14379/iodp.proc.396.2023

Planke, S., Rasmussen, T., Rey, S. S., & Myklebust, R. (2005). Seismic characteristics and distribution of volcanic intrusions and hydrothermal vent complexes in the Vøring and Møre basins. *Geological Society, London, Petroleum Geology Conference Series*, *6*(1), 833–844. https://doi.org/10.1144/0060833

Pogge von Strandmann, P. A. E., Morgan, T. J., West, A. J., Murphy, M. J., Stokke, E. W., Tarbuck, G., et al. (2021). Lithium isotope evidence for enhanced weathering and erosion during the Paleocene-Eocene thermal maximum. *Science Advances*, *7*(42), eabh4224. https://doi.org/10.1126/sciadv.abh4224

Pujalte, V., Baceta, J. I., & Schmitz, B. (2015). A massive input of coarse-grained siliciclastics in the Pyrenean Basin during the PETM: The missing ingredient in a coeval abrupt change in hydrological regime. *Climate of the Past*, *11*(12), 1653–1672. https://doi.org/10.5194/cp-11-1653-2015

Rakshit, S., Dale, A. W., Wallace, D. W., & Algar, C. K. (2023). Sources and sinks of bottom water oxygen in a seasonally hypoxic fjord. *Frontiers in Marine Science*, *10*, 1148091. https://doi.org/10.3389/fmars.2023.1148091

Remmelzwaal, S. R. C., Dixon, S., Parkinson, I. J., Schmidt, D. N., Monteiro, F. M., Sexton, P., et al. (2019). Investigating ocean deoxygenation during the PETM through the Cr isotopic signature of foraminifera. *Paleoceanography and Paleoclimatology*, *34*(6), 917–929. https://doi.org/10.1029/2018PA003372

Robert, C., & Kennett, J. P. (1994). Antarctic subtropical humid episode at the Paleocene-Eocene boundary: Clay-mineral evidence. *Geology*, *22*(3), 211. https://doi.org/10.1130/0091-7613(1994)022<0211:ASHEAT>2.3.CO;2

Röhl, U., Westerhold, T., Bralower, T. J., & Zachos, J. C. (2007). On the duration of the Paleocene-Eocene thermal maximum (PETM). *Geochemistry, Geophysics, Geosystems*, *8*(12), 2007GC001784. https://doi.org/10.1029/2007GC001784

Rosenthal, Y., Lam, P., Boyle, E. A., & Thomson, J. (1995). Authigenic cadmium enrichments in suboxic sediments: Precipitation and post-depositional mobility. *Earth and Planetary Science Letters*, *132*(1–4), 99–111. https://doi.org/10.1016/0012-821X(95)00056-I

Rush, W., Zachos, J., Blackburn, T., & Pogge Von Strandmann, P. A. E. (2025). Continuous sediment sourcing and changes in weathering during the PETM in the Salisbury embayment. *Paleoceanography and Paleoclimatology*, *40*(9), e2025PA005116. https://doi.org/10.1029/2025PA005116

Sandhya, A. G., Longman, J., Struve, T., Jones, M. T., Frieling, J., & Pahnke, K. (2026). Low chemical weathering intensity, enhanced erosion, and euxinic conditions along the Norwegian margin during the Paleocene-Eocene thermal maximum [Dataset]. *Figshare*. https://doi.org/10.6084/m9.figshare.31922955

Sawyer, E. W. (1986). The influence of source rock type, chemical weathering and sorting on the geochemistry of clastic sediments from the Quetico metasedimentary belt, superior province, Canada. *Chemical Geology*, *55*(1–2), 77–95. https://doi.org/10.1016/0009-2541(86)90129-4

Schoon, P. L., Heilmann-Clausen, C., Schultz, B. P., Sinninghe Damsté, J. S., & Schouten, S. (2015). Warming and environmental changes in the eastern North Sea Basin during the Palaeocene–Eocene thermal maximum as revealed by biomarker lipids. *Organic Geochemistry*, *78*, 79–88. https://doi.org/10.1016/j.orggeochem.2014.11.003

Shoenfelt, E. M., Winckler, G., Annett, A. L., Hendry, K. R., & Bostick, B. C. (2019). Physical weathering intensity controls bioavailable primary iron (II) silicate content in major global dust sources. *Geophysical Research Letters*, *46*(19), 10854–10864. https://doi.org/10.1029/2019GL084180

Sluijs, A., Van Roij, L., Harrington, G. J., Schouten, S., Sessa, J. A., LeVay, L. J., et al. (2014). Warming, euxinia and sea level rise during the Paleocene–Eocene thermal maximum on the Gulf Coastal Plain: Implications for ocean oxygenation and nutrient cycling. *Climate of the Past*, *10*(4), 1421–1439. https://doi.org/10.5194/cp-10-1421-2014

Sømme, T. O., Huwe, S. I., Martinsen, O. J., Sandbakken, P. T., Skogseid, J., & Valore, L. A. (2023). Stratigraphic expression of the Paleocene-Eocene thermal maximum climate event during long-lived transient uplift—An example from a shallow to deep-marine clastic system in the Norwegian Sea. *Frontiers in Earth Science*, *11*, 1082203. https://doi.org/10.3389/feart.2023.1082203

Sømme, T. O., Skogseid, J., Sandbakken, P. T., Burgess, R. D., & Anthonissen, E. (2026). Contourite deposits reveal late Paleocene to early Eocene deepwater circulation in the Norwegian-Greenland Sea. *Geology*, *54*(6), 603–608. https://doi.org/10.1130/G54183.1

Stokke, E. W., Jones, M. T., Riber, L., Haflidason, H., Midtkandal, I., Schultz, B. P., & Svensen, H. H. (2021). Rapid and sustained environmental responses to global warming: The Paleocene–Eocene Thermal maximum in the eastern North Sea. *Climate of the Past*, *17*(5), 1989–2013. https://doi.org/10.5194/cp-17-1989-2021

Struve, T., Lamy, F., Gäng, F., Klages, J. P., Kuhn, G., Esper, O., et al. (2026). South Pacific carbon uptake controlled by West Antarctic Ice Sheet dynamics. *Nature Geoscience*, *19*(2), 173–181. https://doi.org/10.1038/s41561-025-01911-0

Svensen, H., Planke, S., Malthe-Sørenssen, A., Jamtveit, B., Myklebust, R., Rasmussen Eidem, T., & Rey, S. S. (2004). Release of methane from a volcanic basin as a mechanism for initial Eocene global warming. *Nature*, *429*(6991), 542–545. https://doi.org/10.1038/nature02566

Sweere, T., Van Den Boorn, S., Dickson, A. J., & Reichart, G.-J. (2016). Definition of new trace-metal proxies for the controls on organic matter enrichment in marine sediments based on Mn, Co, Mo and Cd concentrations. *Chemical Geology*, *441*, 235–245. https://doi.org/10.1016/j.chemgeo.2016.08.028

Takei, H., Yokoyama, T., Makishima, A., & Nakamura, E. (2001). Formation and suppression of AlF_3 during HF digestion of rock samples in Teflon bomb for precise trace element analyses by ICP-MS and ID-TIMS. *Proceedings of the Japan Academy, Series B*, *77*(1), 13–17. https://doi.org/10.2183/pjab.77.13

Tanaka, E., Yasukawa, K., Ohta, J., & Kato, Y. (2022). Enhanced continental chemical weathering during the multiple early Eocene hyperthermals: New constraints from the southern Indian Ocean. *Geochimica et Cosmochimica Acta*, *331*, 192–211. https://doi.org/10.1016/j.gca.2022.05.022

Taylor, S. R., & McLennan, S. M. (1985). *The Continental crust: Its composition and evolution*. Blackwell Scientific Publications

Tierney, J. E., Zhu, J., Li, M., Ridgwell, A., Hakim, G. J., Poulsen, C. J., et al. (2022). Spatial patterns of climate change across the Paleocene–Eocene thermal maximum. *Proceedings of the National Academy of Sciences*, *119*(42), e2205326119. https://doi.org/10.1073/pnas.2205326119

Tossell, J. A. (2005). Calculating the partitioning of the isotopes of Mo between oxidic and sulfidic species in aqueous solution. *Geochimica et Cosmochimica Acta*, *69*(12), 2981–2993. https://doi.org/10.1016/j.gca.2005.01.016

Trapp-Müller, G., Caves Rugenstein, J., Conley, D. J., Geilert, S., Hagens, M., Hong, W.-L., et al. (2025). Earth's silicate weathering continuum. *Nature Geoscience*, *18*(8), 691–701. https://doi.org/10.1038/s41561-025-01743-y

Tribovillard, N., Algeo, T. J., Lyons, T., & Riboulleau, A. (2006). Trace metals as paleoredox and paleoproductivity proxies: An update. *Chemical Geology*, *232*(1–2), 12–32. https://doi.org/10.1016/j.chemgeo.2006.02.012

Vickers, M. L., Jones, M. T., Longman, J., Evans, D., Ullmann, C. V., Wulfsberg Stokke, E., et al. (2024). Paleocene–Eocene age glendonites from the Mid-Norwegian Margin – Indicators of cold snaps in the hothouse? *Climate of the Past*, *20*(1), 1–23. https://doi.org/10.5194/cp-20-1-2024

Walters, G. L., Kemp, S. J., Hemingway, J. D., Johnston, D. T., & Hodell, D. A. (2022). Clay hydroxyl isotopes show an enhanced hydrologic cycle during the Paleocene-Eocene thermal maximum. *Nature Communications*, *13*(1), 7885. https://doi.org/10.1038/s41467-022-35545-2

Wei, G.-Y., Pohl, A., Jiang, S., Zhang, H., Wang, W., Pogge, A. E., et al. (2025). Changes in continental weathering regimes inhibited global marine deoxygenation during the Paleocene-Eocene thermal maximum. *Nature Communications*, *16*(1), 9163. https://doi.org/10.1038/s41467-025-64217-0

Westerhold, T., Röhl, U., Laskar, J., Raffi, I., Bowles, J., Lourens, L. J., & Zachos, J. C. (2007). On the duration of magnetochrons C24r and C25n and the timing of early Eocene global warming events: Implications from the ocean drilling program leg 208 Walvis Ridge depth transect. *Paleoceanography*, *22*(2), 2006PA001322. https://doi.org/10.1029/2006PA001322

Wieczorek, R., Fantle, M. S., Kump, L. R., & Ravizza, G. (2013). Geochemical evidence for volcanic activity prior to and enhanced terrestrial weathering during the Paleocene Eocene thermal maximum. *Geochimica et Cosmochimica Acta*, *119*, 391–410. https://doi.org/10.1016/j.gca.2013.06.005

Wignall, P. B., & Twitchett, R. J. (1996). Oceanic Anoxia and the end Permian mass extinction. *Science*, *272*(5265), 1155–1158. https://doi.org/10.1126/science.272.5265.1155

Winguth, A. M. E., Thomas, E., & Winguth, C. (2012). Global decline in ocean ventilation, oxygenation, and productivity during the Paleocene-Eocene thermal maximum: Implications for the benthic extinction. *Geology*, *40*(3), 263–266. https://doi.org/10.1130/G32529.1

Zeebe, R. E., & Lourens, L. J. (2019). Solar system chaos and the Paleocene–Eocene boundary age constrained by geology and astronomy. *Science*, *365*(6456), 926–929. https://doi.org/10.1126/science.aax0612

Zhang, K., Stüeken, E. E., Thomazo, C., Zhao, Z., Minyuk, P. S., Cai, S., et al. (2025). Volcanic ash drives contrasting redox shifts and biogeochemical feedbacks in ancient marine and lacustrine systems. *Communications Earth & Environment*, *6*(1), 850. https://doi.org/10.1038/s43247-025-02821-0

Zhang, Y., Pe-Piper, G., & Piper, D. J. W. (2014). Sediment geochemistry as a provenance indicator: Unravelling the cryptic signatures of polycyclic sources, climate change, tectonism and volcanism. *Sedimentology*, *61*(2), 383–410. https://doi.org/10.1111/sed.12066